

Synergistic Steric and Electronic Effects on the Photoredox Catalysis by a Multivariate Library of Titania Metal–Organic Frameworks

Jacob T. Bryant,[¶] Matthew W. Logan,[¶] Zhihengyu Chen, Marcus Djokic, Daniel R. Cairnie, Demetrius A. Vazquez-Molina, A. Nijamudheen, Kyle R. Langlois, Michael J. Markley, Gisselle Pombar, Ashley A. Holland, Jonathan D. Caranto, James K. Harper, Amanda J. Morris,^{*} Jose L. Mendoza-Cortes,^{*} Titel Jurca,^{*} Karena W. Chapman,^{*} and Fernando J. Uribe-Romo^{*}



Cite This: *J. Am. Chem. Soc.* 2023, 145, 4589–4600



Read Online

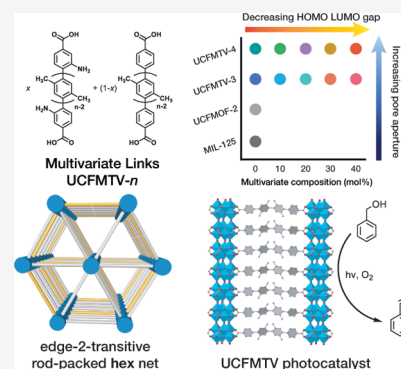
ACCESS |

Metrics & More

Article Recommendations

Supporting Information

ABSTRACT: Metal–organic frameworks (MOFs) that display photoredox activity are attractive materials for sustainable photocatalysis. The ability to tune both their pore sizes and electronic structures based solely on the choice of the building blocks makes them amenable for systematic studies based on physical organic and reticular chemistry principles with high degrees of synthetic control. Here, we present a library of eleven isorecticular and multivariate (MTV) photoredox-active MOFs, UCFMOF-*n*, and UCFMTV-*n*-*x*% with a formula $\text{Ti}_6\text{O}_9[\text{links}]_3$, where the links are linear oligo-*p*-arylene dicarboxylates with *n* number of *p*-arylene rings and *x* mol% of multivariate links containing electron-donating groups (EDGs). The average and local structures of UCFMOFs were elucidated from advanced powder X-ray diffraction (XRD) and total scattering tools, consisting of parallel arrangements of one-dimensional (1D) $[\text{Ti}_6\text{O}_9(\text{CO}_2)_6]_\infty$ nanowires connected through the oligo-arylene links with the topology of the edge-2-transitive rod-packed hex net. Preparation of an MTV library of UCFMOFs with varying link sizes and amine EDG functionalization enabled us to study both their steric (pore size) and electronic (highest occupied molecular orbital–lowest unoccupied molecular orbital, HOMO–LUMO, gap) effects on the substrate adsorption and photoredox transformation of benzyl alcohol. The observed relationship between the substrate uptake and reaction kinetics with the molecular traits of the links indicates that longer links, as well as increased EDG functionalization, exhibit impressive photocatalytic rates, outperforming MIL-125 by almost 20-fold. Our studies relating photocatalytic activity with pore size and electronic functionalization demonstrate how these are important parameters to consider when designing new MOF photocatalysts.



INTRODUCTION

Photoredox-active materials are those in which light excitation produces charge-separated states that can catalyze the oxidation or reduction of substrates.^{1,2} This class of compounds constitutes the majority of photocatalysts, existing both in molecular (e.g., $\text{Ru}(\text{bpy})_3^{+2}$)³ and extended (TiO_2)⁴ forms and under both homogeneous and heterogeneous conditions. Metal–organic frameworks (MOFs) that are photoredox active are very attractive for sustainable photocatalysis because they combine the advantages of molecular homogeneous and heterogeneous photocatalysts.⁵ As for molecular homogeneous photocatalysts, the design of the ligand plays a major role in moderating the catalytic activity. As for heterogeneous catalysts, this activity is highly dependent on surface areas and available reactive sites and is commonly made of recoverable and reusable, earth-abundant materials.^{6–8}

Titania MOFs are ideal platforms to study tunable photocatalysis because of the synergy observed between the electronic structure of functional organic links and the d-states of Ti^{4+} in the secondary building units (SBUs), promoting the formation of long-lived charge-separated states required for

photocatalysis.^{9–17} From a physical organic view, it is possible to design organic links in a modular fashion to probe the photoredox effect as a function of the linker structure. For example, the electronic effects that allow the charge-separated states to form can be elucidated by varying the electron-donating/withdrawing ability of functional groups as it has been performed in MIL-125.^{12,14,15} These effects can be characterized by the highest occupied molecular orbital–lowest unoccupied molecular orbital (HOMO–LUMO) gaps and excited-state lifetimes that depend on the electronic structures of the MOFs and can be correlated to their photocatalytic performance. Likewise, the steric effects can be probed by systematically varying the molecular size of the links

Received: November 16, 2022

Published: February 16, 2023



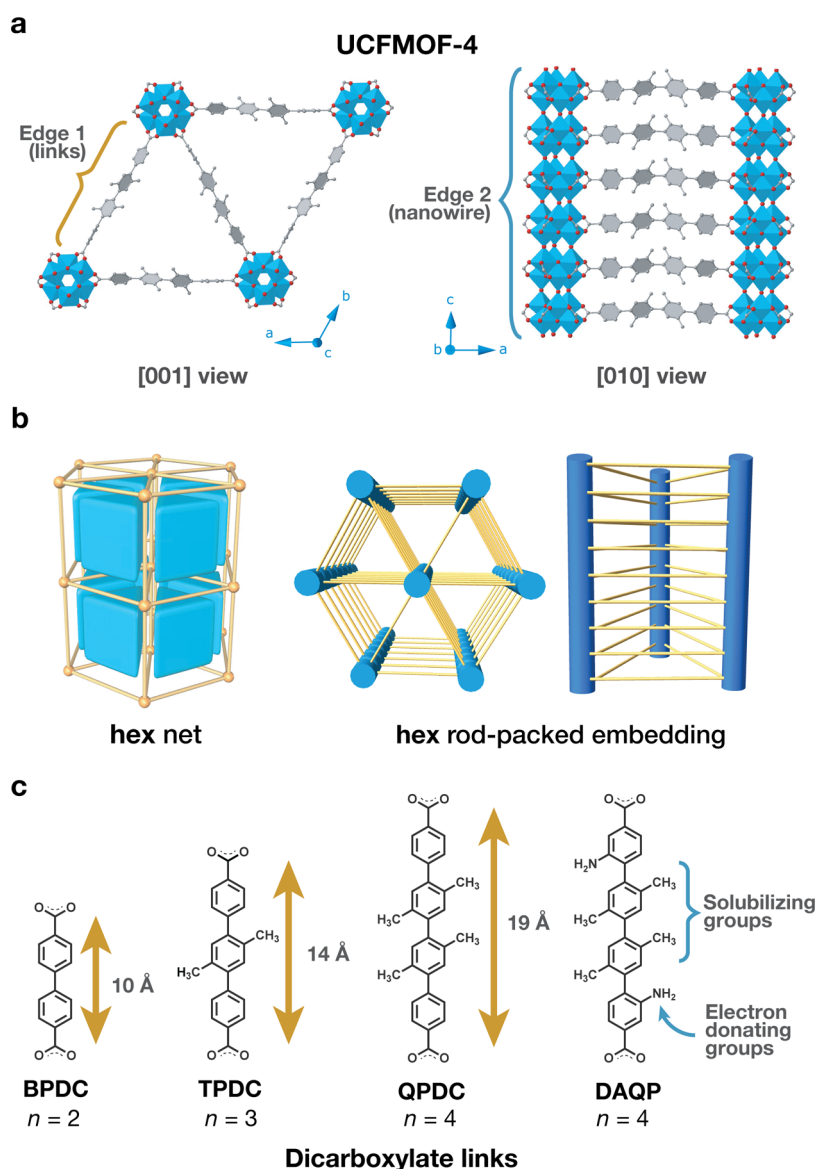


Figure 1. (a) Atomic structure of UCFMOF-4 viewed from two directions to illustrate the two types of edges. Blue, titanium; red, oxygen; gray, carbon. Hydrogen atoms are omitted for clarity, and arylene rings are highlighted for visualization. (b) 3D renderings of the **hex** net in its maximum symmetry embedding (left) and its rod-packed embedding (center and right). (c) Dicarboxylate organic links used in this study, featuring increased carboxylate–carboxylate distances, solubilizing, and electron-donating groups.

via sequential addition of 1,4-phenylene units between the points of extension.¹⁸ This would result in MOF photocatalysts with varied pore sizes and apertures that will affect the rates and modes in which substrates are adsorbed and photo-transformed.

Another advantage that MOFs offer is the ability to prepare isorecticular and multivariate systems. From a reticular chemistry perspective, MOFs amenable for isorecticular expansion and multivariates are those with simple structures and have nets with topologies that follow the minimal transitivity principle.¹⁹ This principle is founded on treating nets mathematically as graphs of vertices and edges with a given transitivity that indicate the unique kinds of vertices, edges, faces, and tiles present in the net.²⁰ The advantage of using reticular chemistry as a guide for design is that vertices, edges, faces, and tiles represent designable components of the framework: SBUs, links, pore apertures, and pore shapes, respectively. By focusing on nets that have only one kind of

edge (edge-1-transitive nets), it is very easy to prepare isorecticular frameworks simply by varying the length of the links (isorecticular principle).²¹ Similarly, by having only one kind of edge, mixtures of links with identical geometry and metrics but different degrees of functionalization can also form isorecticular mixtures as multivariate (MTV) frameworks. In MTVs, different links of similar size and geometry will compete and try to occupy the same edge position during crystallization. This will favor the formation of phases similar to inorganic substitutional solid solutions.²² Studying MTV frameworks with the same degree of chemical control as inorganic solid solutions enables emergent relationships between the composition and observation of the solid-state photoredox property.

In this work, we present a synthetic, crystallographic, computational, photophysical, and photocatalytic study of a library of eleven isorecticular **hex** rod-packed MOF photocatalysts based on a new titania MOF that we name

UCFMOFs and UCFMTVs with a formula $\text{Ti}_6\text{O}_9[\text{links}]_3$ (Figure 1a). These MOFs are made of two kinds of edges: the organic links (edge 1) and a titania nanowire SBU that is a 1-periodic titanium oxocarboxylate cluster (edge 2). This SBU has been previously observed in MOFs like MIL-177HT²³ and ZSTU-1, -2, and -3,²⁴ all of which are made with nonlinear links. In our case, the nanowire SBUs align parallel to each other connected through the linear organic links in a hex-rod net topology.²⁵ The hex net, in its maximum symmetry embedding, forms by tiling the space with trigonal prisms (Figure 1b) and has two kinds of edges. In the frameworks presented here, one of the edges corresponds to the rod SBU (blue rods) and the second to the organic links (golden sticks). In its rod-packed form, there is only one kind of edge for the organic links and thus likely to allow isorecticular expansions and multivariates. The links also feature methyl-solubilizing groups as well as amine electron-donating groups (EDGs) as MTVs (Figure 1c).^{13,15,17} Powder diffraction crystallography in tandem with a detailed local structure characterization of the titania SBU through pair distribution function (PDF) enabled the elucidation of both their average and local structure. In turn, accurate crystal structures allowed the calculation of their electronic band structures and band gaps using high-level density functional theory (DFT) methods that match experimental observations. Substrate adsorption kinetics and photocatalytic studies using the oxidation of benzyl alcohol demonstrated the composition–structure–property relationships between the size and the content of MTV links and the photoredox property of the MOF. MOFs with a larger pore size and a moderate amine content exhibited enhanced photoredox activity related to their steric and electronic structures.

RESULTS AND DISCUSSION

Solvothermal reaction of a molecular titanium precursor $\text{Ti}_8\text{O}_8(\text{tBuCO}_2)_{16}$ with H_2BPDC in *N,N*-diethylformamide (DEF) in a microwave reactor at 120 °C for 1 h yielded UCFMOF-2 (Scheme 1). Solvothermal reaction with H_2TPDC , or H_2QPDC in *N,N*-dimethylformamide (DMF) in an isothermal oven at 150 °C for 4 d, resulted in the formation of UCFMOF-3, and UCFMOF-4, respectively. We found that including methyl groups in the central rings of TPDC and QPDC favored solubility, and in combination with using mildly reactive titanium sources, such as

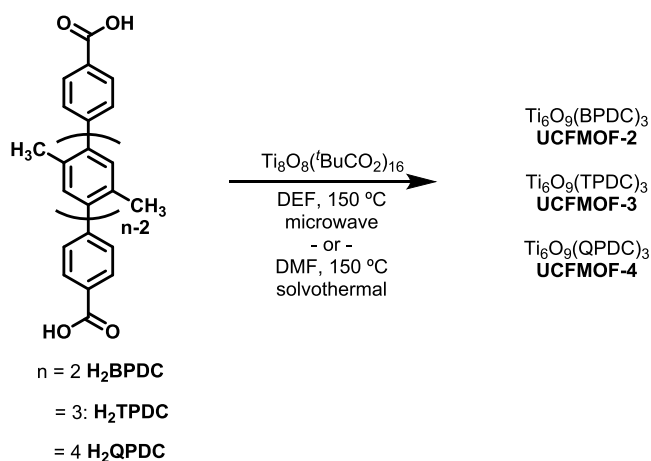
$\text{Ti}_8\text{O}_8(\text{tBuCO}_2)_{16}$,²⁶ produced samples that display the highest performance for photocatalysis. Using other titanium sources, such as $\text{Ti}(\text{OiPr})_4$, $\text{Ti}(\text{OBu})_4$, TiCl_4 , or other molecular clusters,²⁷ as well as higher oven or microwave temperatures, also produce crystalline MOFs (Figure S3). Our optimized conditions resulted in MOF samples with the highest surface areas and the greatest catalytic activity. For UCFMOF-2, only microwave conditions produced crystalline samples.

Scanning electron microscopy (SEM, Figure 2a, Section S7) revealed microcrystalline powders containing nanosized rod-like crystallites of homogeneous shape and size distribution. Powder X-ray diffraction exhibited highly crystalline MOFs with an isorecticular trend evidenced by the low-angle shift in their first diffraction peak from $d = 15.03$ Å in UCFMOF-2 to 19.79 Å in UCFMOF-3 and 23.51 Å in UCFMOF-4 (Figure 2b). Indexing of the PXRD patterns indicated hexagonal unit cells with *a*-parameter that varied from 17.419(19) to 22.9387(24) and 27.231(32) Å, respectively, with different *c*-parameter in all of the cases (*c* = 6.353(15), 5.9616(47), 4.224(11) Å, respectively, Table S3). Full pattern decomposition in GSAS-II,²⁸ followed by electron density map reconstruction with Superflip,²⁹ and Chimera,³⁰ resulted in electron density maps that indicate the presence of 1D metal oxide SBUs at the origin of the cell and along the *c*-direction that are separated by a full linker length in all 6 directions in the *ab* plane, resembling the hex rod net (Figure 2c).²⁵

The SBU in this net is very different from the 0-periodic octameric cluster in the titanium SBU of MIL-125, indicating that these clusters restructure during synthesis. The only examples of 6-connected titania SBUs are found in MIL-177HT,²³ ZSTU MOFs,²⁴ MIL-177LT,²³ and MOF-901.²⁷ The first two examples are MOFs made with tri- and tetracarboxylate links that connect to a $[\text{Ti}_6\text{O}_9(\text{CO}_2)_6]_\infty$ nanowire SBU (Figure 2d). The other possibility is a hexameric $[\text{Ti}_6\text{O}_6(\text{OiPr})_6(\text{CO}_2)_6]$ SBU observed in MOF-901 and MIL-177LT, which is 0-periodic, and contains alkoxide chains as capping groups. ¹³C cross-polarization with magic-angle-spinning (CP MAS) NMR spectra of all three UCFMOFs showed the presence of only the organic links with no signals for alkoxides, solvents, *t*BuCO₂, or other organic species (Figure S24–S27), suggesting that the alkoxide-free $[\text{Ti}_6\text{O}_9(\text{CO}_2)_6]_\infty$ nanowire is a reasonable SBU model.

The local structure of the titania SBU was verified based on pair distribution function (PDF) analysis of X-ray total scattering data. The PDF is sensitive to the distribution of atom distances. By comparing PDFs of UCFMOFs and other titania MOFs^{23,24,27,31} and clusters²⁶ (Section S4), a close correspondence was identified between the 1D columns in all UCFMOFs and the $[\text{Ti}_6\text{O}_9(\text{CO}_2)_6]_\infty$ 1D cluster (Figure 2d). In UCFMOFs, $[\text{Ti}_6\text{O}_6]_\infty$ subunits (Figure 2e) are connected together by three oxo-bridges to form a column, and then the columns are linked together in the *ab* directions by carboxylate links in a hexagonal cell. Peaks in the PDF at *ca.* 1.2, 2.0, and 3.1 Å belong to the C–O/C–C, Ti–O, and Ti–Ti distances, respectively (Table S5–7). PDFs confirmed the presence of infinite $[\text{Ti}_6\text{O}_9(\text{CO}_2)_6]_\infty$ SBUs in UCFMOF-3 and UCFMOF-4 by displaying peaks at 3.12 and 4.66 Å, which are Ti–Ti pair distances at a Ti_4O_4 quadrilateral face of the clusters and Ti–Ti distances at a Ti_6O_6 body diagonal. To further understand the local structure of the titania columns, a differential PDF³² (Figures 2e, and S18–S20) was obtained by subtracting the PDF measured for the organic links from the PDF of the MOFs and then fitting this d-PDF that isolated the inorganic

Scheme 1



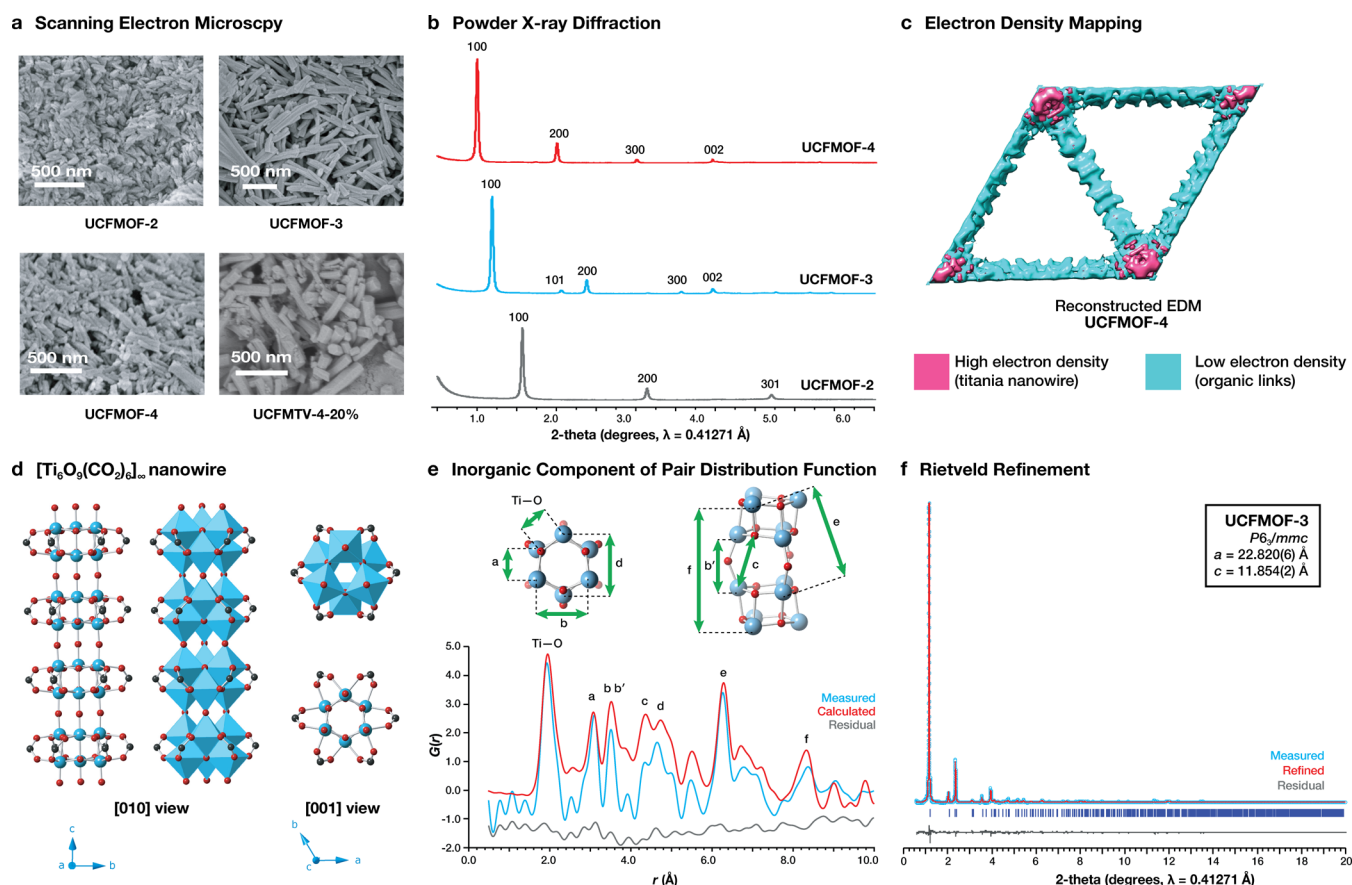


Figure 2. Structural characterization of UCFMOFs. (a) Scanning electron micrographs indicating the rod-like shape of the crystallites, scale is included. (b) Indexed X-ray powder diffractograms, collected at 11-BM beamline at APS, hkl indices are indicated. (c) Reconstructed electron density map of UCFMOF-4 obtained with Superflip and Chimera, displaying regions of high (pink) and low (blue) electron densities, contrasting titanium oxide vs organic sites. (d) Molecular structure of the titania oxocarboxylate nanowires from two crystallographic views. Blue, titanium; red, oxygen; black, carbon. (e) Inorganic component of the PDF of UCFMOF-3 indicating atomic distances within the SBU. (f) Rietveld refinement plot of UCFMOF-3, displaying the measured (blue), refined (red) patterns, residuals (gray), and Bragg reflections (blue ticks) refined lattice parameters, and space group are indicated.

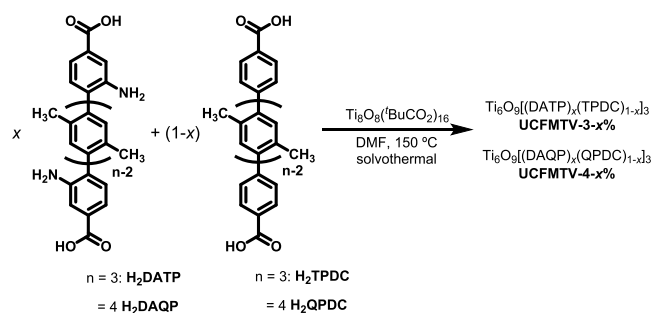
part of the MOF with the $[\text{Ti}_6\text{O}_9(\text{CO}_2)_6]_\infty$ column model (Figure 2e). Comparing UCFMOF-2 to UCFMOF-3 and UCFMOF-4, Ti–O–Ti bonds connecting two $\text{Ti}_6\text{O}_9(\text{CO}_2)_6$ clusters have a broader angle, and Ti–O–Ti bonds in the six-member ring have a narrower angle. These likely contribute to the differences in c -parameter for the different MOFs. Meanwhile, Fourier transform of PDFs confirms the existence of 1D titania column SBUs and the distance between them (Figures S21–S23).

We used the $[\text{Ti}_6\text{O}_9(\text{CO}_2)_6]_\infty$ cluster to generate crystal models in the Forcite module in Materials Studio³³ producing unit cells with lattice parameters and simulated diffraction patterns similar to those observed experimentally. The combination of crystal modeling with high-resolution local structure studies yielded an average unit cell for each of the MOFs with high-symmetry $P6_3/mmc$ space groups based on the proposed hex rod net. Application of the Rietveld method in GSAS-II to synchrotron PXRD data resulted in convergent refinements with lattice parameters and residuals: $a = 22.820(6) \text{ \AA}$, $c = 11.850(20) \text{ \AA}$, $R_p = 7.48\%$, $\chi^2 = 1.92$ for UCFMOF-3 (Figure 2f) and $a = 26.750(17) \text{ \AA}$, $c = 11.760(5) \text{ \AA}$, $R_p = 8.77\%$, $\chi^2 = 1.95$ for UCFMOF-4 (Table S4). Low profile residuals in UCFMOF-3 and UCFMOF-4 indicate high accuracy in the crystal structure refinements that enable MTV synthesis and characterization of both the steric effects in the

pore and their electronic structures. UCFMOF-2 did not provide refinements with low residuals due to observed impurities in contrast to UCFMOF-3 and UCFMOF-4. Therefore, we present UCFMOF-2 as an indexed model from DFT (Table S13).

Scheme 2 describes the preparation of the multivariate series UCFMTV-3- $x\%$ and UCFMTV-4- $x\%$, where x indicates the mol% content of the diamino links DATP and DAQP, respectively. The links were prepared by modular synthesis, performing nitration/reduction on the benzoate endpiece (Schemes S1 and S2), while retaining the alkylated core for

Scheme 2



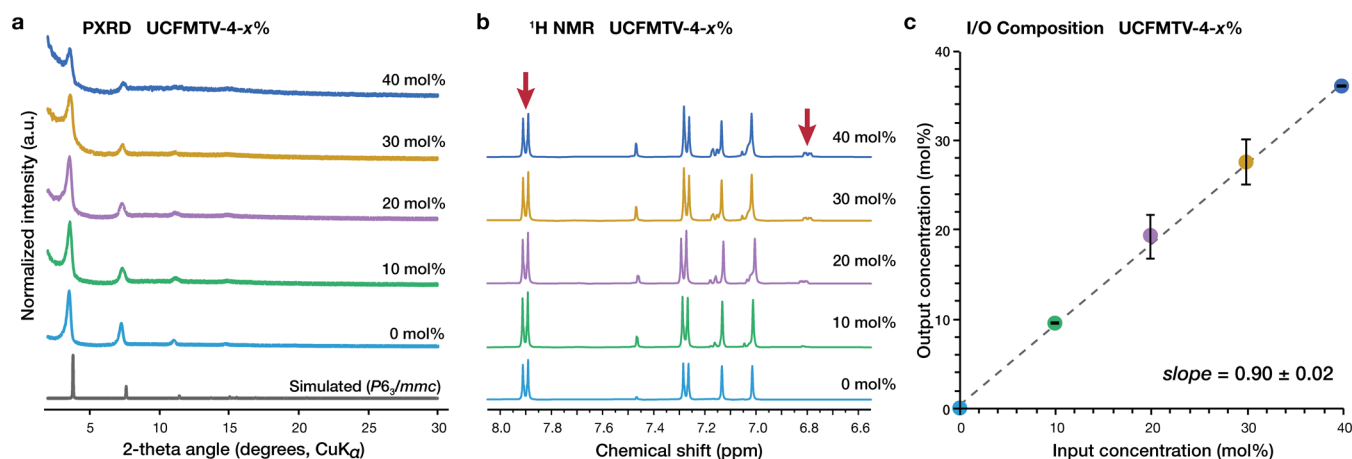


Figure 3. Composition analysis of UCFMTVs. (a) PXRD of UCFMTV-4-*x*% compared to simulated UCFMOF-4, **DAQP** content in mol% is indicated. (b) Solution ¹H NMR of digested UCFMTV-4 (KF, D₂O, DMSO-*d*₆, rt), arrows indicate the signals used for quantification. (c) Input–output (I/O) plot of UCFMTV-4 up to 40% **DAQP**. I/O slope is indicated, error bars are from triplicate measurements.

solubility. These two links contain two amino substituents as EDGs specifically selected to enhance cooperation between links and the titania SBU. In both MTV series, we observed crystal formation up to 40 mol% **DATP/DAQP** content, according to their PXRD patterns (Figures 3a, S12, and S13), SEM micrographs (Figure 2a), and ¹H NMR spectra of base-digested samples (Figure 3b). Concentrations of 50 mol% and higher produced samples with poor diffraction and low yield were not further studied. We speculate that steric crowding by amino groups in the pore reduces the tolerance of MTV formation and/or promotes defects, as observed in other MTV MOFs.³⁴ From the integration of the NMR spectra, we constructed input/output (I/O) composition plots (Figures 3c, S1, and S2) that indicate the trends at which the MTV links incorporate into the framework with respect to an expected composition. The I/O plots of UCFMTV-3 and UCFMTV-4 displayed linear trends with a nearly 1:1 ratio of incorporation, exhibiting slopes of 1.04 ± 0.07 for UCFMTV-3 and 0.90 ± 0.02 for UCFMTV-4. These slopes indicate that the MTV system resembles a partial solid solution up to 40 mol%,²² meaning that both links can incorporate into the MOF below this upper limit of composition at the specified input ratios.

The electronic properties of all UCFMTVs, including optical HOMO–LUMO gap, were determined by diffuse reflectance ultraviolet–visible spectroscopy (DR-UV–vis, Figure 4). Optical HOMO–LUMO gaps were determined through application of the Tauc model to the UV–vis spectra (Section S10). All of the UCFMTVs exhibit strong absorption bands in the UV region. Absorption spectra for UCFMTV-3-0% show no features above 400 nm while increasing **DATP** mol% results in an incremental bathochromic shift in the most prominent peak from around 250 nm to around 370 nm, accompanied by the evolution of a broad shoulder above 400 nm. This broad feature is especially prominent in UCFMTV-3-40% (Figure 4a), exhibiting residual absorption as far as 700 nm. In UCFMTV-4-*x*%, a similar general trend is evident with increasing **DAQP** content (Figure 4b) but with a less dramatic red-shift broadening. Instead, intermediate compositions (10–30 mol%) exhibit very similar absorption spectra. The obtained HOMO–LUMO gaps (E_g) decrease from $E_g = 3.46$ eV in UCFMTV-3-0% to 1.80 eV in UCFMTV-3-40% and from $E_g = 3.57$ eV in UCFMTV-4-0% to 1.93 eV in UCFMTV-4-40% (Table 1). In UCFMTV-3, the change is sequential, whereas in

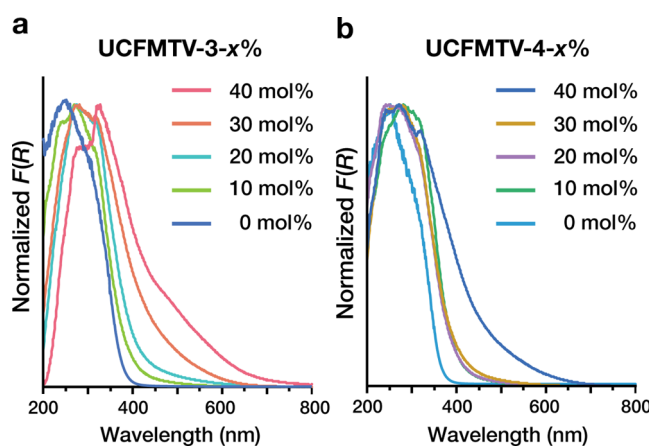


Figure 4. Diffuse reflectance UV–visible spectra of (a) UCFMTV-3 and (b) UCFMTV-4. **DAQP/DATP** content in mol% is indicated. UCFMOF-3 and UCFMOF-4 correspond to UCFMTV-*n*-0%.

Table 1. HOMO–LUMO Gaps of UCFMTVs

<i>x</i> (mol%)	HOMO–LUMO gap (eV)	
	UCFMTV-3- <i>x</i> %	UCFMTV-4- <i>x</i> %
0	3.46	3.57
10	2.78	2.80
20	2.36	2.77
30	2.13	2.68
40	1.80	1.93

UCFMTV-4, the HOMO–LUMO gaps at intermediate concentrations are clustered between $E_g = 2.68$ to 2.80 eV. Density functional theory (DFT) calculations of the electronic structure of UCFMTVs were performed at both the unrestricted B3LYP^{35,36} and HSE06³⁷ exchange–correlation functional level with Grimme-D3³⁸ dispersion correction (Section S13). HSE06 tends to reproduce the most accurate band gap calculations, where it slightly underestimates experimental results; meanwhile, B3LYP tends to slightly overestimate them.³⁹ HSE06-D3 predicts gaps of $E_g = 3.24$ and 3.27 eV for UCFMOF-3 and UCFMOF-4, respectively. B3LYP-D3, on the other hand, predicts gaps of $E_g = 3.65$ and 3.53. Together, these match well with the observed values in UCFMTV-0%. Calculations performed in a hypothetical

UCFMTV-4-100% (100 mol% **DAQP**) predict a B3LYP-D3 energy gap of 2.91 eV and an HSE06-D3 gap of 2.67 eV, matching well with experimental results for UCFMTV-4 between 10 and 30% **DAQP** content. Interestingly, the gaps of both UCFMTVs at 40 mol% EDG are much lower than the predicted values, suggesting that higher concentrations of **DATP/DAQP** may induce an increase of optically active defects.

All of the UCFMTVs in our library are microporous as determined by their N_2 adsorption measurements at 77 K. All isotherms exhibited sharp uptakes at low pressure, followed by saturation and characteristic of IUPAC type II isotherms (Section S6). Application of the Brunauer–Emmet–Teller (BET) model in pressure ranges as determined by Rouquerol plot analysis produced BET surface areas shown in Table S8.⁴⁰ For UCFMTV-3, the BET surface areas decrease from 1780 $m^2 g^{-1}$ for UCFMTV-3-0% to 850 $m^2 g^{-1}$ for UCFMTV-3-40%. Similarly, for UCFMTV-4, increasing **DAQP** content results in a decrease in the BET surface area from 2430 $m^2 g^{-1}$ for UCFMTV-4-0% to 1320 $m^2 g^{-1}$ for UCFMTV-4-30%. This result is expected because of increased deadweight and dead volume from the $-NH_2$ functional groups.

Fitting nonlocal density functional theory (NLDFT) models to the experimental isotherms produced pore size distribution (PSD) plots (Figure 5a and Section S6) with average pore sizes of 10.6 Å for UCFMOF-3 and 13.1 Å for UCFMOF-4. PSD for UCFMTV-3-*x*% shows average pore diameters from 10.6 to 13.4 Å with an increase in contribution from larger pore sizes ranging from 11.3 to 12.4 Å, consistent with increased **DATP** content. In the case of UCFMTV-4-*x*%, increased **DAQP** exhibited the same main average pore size; however, we also observed an increase in contribution by a larger pore at 14.9 Å (Figure 3f). The increase of this second pore size contribution suggests an incremental appearance of defects with increased amino content. Trends observed with NLDFT show a relationship between an increase in total pore volume with increased linker size and decreased volume with increased **DAQP/DATP** content.

The pore structure of a MOF determines its ability to adsorb and transport substrates and products. It provides an accurate picture of the steric environment inside the pores, and it is characterized by the distinctive pore shapes and their distribution of diameters. It is obtained by comparing average pore sizes from PSD plots from gas adsorption with those observed in the refined crystal structure from X-ray diffraction, as first demonstrated by Sudik et al.⁴¹ From the refined structures, we observe a single 1D pore with trigonal prismatic shape and apertures that increase from *ca.* 7–14 Å in UCFMTV-3 to *ca.* 7–17 Å in UCFMTV-4, consistent with NLDFT-derived pore sizes. One-dimensional (1D) pores offer the advantage of forming narrow unimodal distributions in the PSD plot. In contrast, MIL-125 is a MOF with *fcu* net. This net contains a 3-dimensional pore system with two shapes (tetrahedral and octahedral) and narrow pore windows. In the *hex* rod net, however, continuous one-dimensional pores allow for simpler diffusion pathways and easier access to active catalytic sites. Furthermore, the parallel arrangement of *p*-arylene links contains an environment inside the pore that is highly aromatic (like toluene or xylene) and should interact favorably with aromatic substrates like benzyl alcohol (**BzOH**).

Determination of the adsorption kinetics by substrates provides a measure at which they load, diffuse, and access active photocatalytic sites. It also helps us to observe trends in

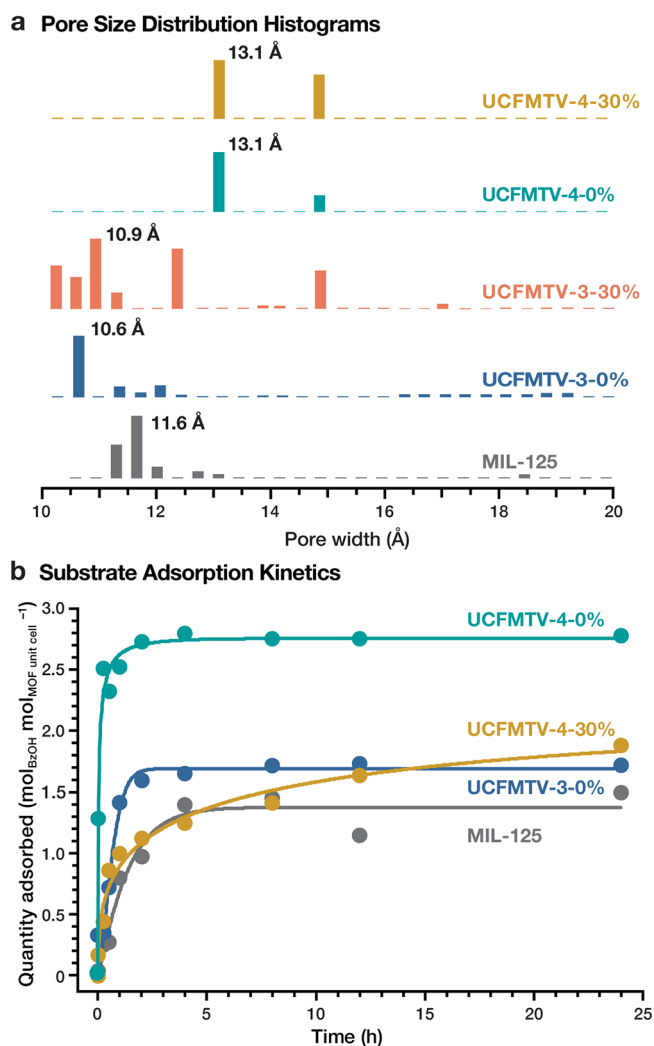


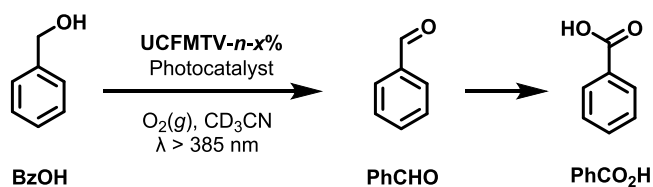
Figure 5. (a) Pore size distribution histograms for MIL-125 (gray), UCFMTV-3-0% (blue), UCFMTV-3-30% (red), UCFMTV-4-0% (turquoise), and UCFMTV-4-30% (gold). (b) Solution adsorption kinetics plot of **BzOH** uptake in MIL-125, UCFMTV-3-0%, UCFMTV-4-0%, and UCFMTV-4-30% (same colors). Line was obtained from fittings (see the Supporting Information).

total substrate uptake and kinetic rates with respect to the MOF photocatalysts. Measurement of the solution adsorption kinetic plots of **BzOH** into UCFMTVs and MIL-125 from acetonitrile (MeCN, $C_0 = 250$ mM) was followed by 1H NMR in a batch reactor in the dark by sampling over time at increased intervals. Figure 5b shows the adsorption kinetics in units of mol of **BzOH** per mol of MOF unit cells vs. time, which is equivalent to molecules of **BzOH** per unit cell vs time. UCFMOF-3, UCFMOF-4, and MIL-125 observed sharp uptakes at early times followed by saturation at around 5 h. UCFMTV-4-30%, in contrast, shows uptake well below saturation after 24 h (Figure 5b yellow trace), reaching equilibrium at a slower rate than the 0% MOFs. Fitting of fractal-like Langmuir adsorption kinetic models to the experimental data resulted in low residuals (Section S11). Fractal-like kinetics⁴² indicate that the mechanism of adsorption involves multiple pathways and that the values of k_{ads} and k_{des} are time-dependent. Instead, the fitted constants k_1 and k_2 —different from k_{ads} and k_{des} —only provide a qualitative measure of the rates.⁴³ We observe a direct correlation of fitted

uptake at equilibrium (q_e) with pore size and an inverse trend with increased DAQP content. Substrate saturation uptakes at an equilibrium increase from $q_e = 1.412(1)$ molecules per unit cell in MIL-125 to $2.806(7)$ molecules per unit cell in UCFMOF-4. A grand canonical Monte Carlo (GCMC) simulation (see computational details in Section S13) of BzOH adsorption using the Sorption module in Materials Studio⁴⁴ revealed an average uptake of 10–20 molecules per unit cell in all of the modeled MOFs (Figures S99–S103). This suggests that there is available space within the pores in all four MOFs for the substrate to load, with differences in adsorption related to the diffusion mechanisms, such as in MIL-125, in which loading is restricted due to small pore apertures.

After establishing successful BzOH adsorption into the MOFs, we followed its aerobic photocatalyzed oxidation (Scheme 3) under broadband visible light irradiation in a

Scheme 3



batch reactor (Xe lamp) with $\lambda > 385$ nm to avoid UV-generated hydroxyl radicals.¹³ Reaction kinetics were followed using ¹H NMR of samples collected over time using mesitylene as an internal standard (Figure 6a and Section S12). Two major products were observed: benzaldehyde (PhCHO) by its aldehyde ¹H signal ($\delta = 10$ ppm) after 12 h and benzoic acid (PhCO₂H) by its aromatic proton signal ($\delta = 8.2$ ppm) after 36 h. At the same time, a decrease in the methylene signal from BzOH ($\delta = 4.5$ ppm) was observed in as little as 2 h. The difference in time points at which the reactants disappear and the products appear may relate to (1) preferential adsorption of the products or (2) possible slow in-pore substrate diffusion.

A solution adsorption experiment (Figure S77), where equimolar amounts of BzOH, PhCHO, and PhCO₂H were loaded into UCFMOF-4, demonstrated that PhCHO has a higher affinity for this MOF than BzOH or PhCO₂H, indicating preferential adsorption of the product. A photocatalytic experiment, where PhCHO was used as a substrate in UCFMOF-4, indicated full transformation to PhCO₂H after 12 h. This observation indicates that it is very likely that the PhCO₂H we observe was formed from photooxidation of intermediate PhCHO rather than direct oxidation of BzOH, emphasizing the need for efficient product removal before overoxidation under extended irradiation periods. Integration of all NMR signals with respect to the internal standard produced photocatalytic plots shown in Figure 6b as turnover number ($\text{mol}_{\text{prod}} \text{mol}_{\text{MOF unit cell}}^{-1}$) vs time (h). The obtained kinetic plots observed a linear trend of product formation vs. time, indicating pseudo-zero order reaction kinetics, consistent with photoredox processes, where electron transfer is the rate-limiting step. We observe a direct relationship between the pseudo-zero order turnover rate k_0 and pore aperture as well as the degree of functionalization (Table S12).

The most practical relationship was found by comparing turnover rate (k_0) vs substrate loading at 24 h (q_{24}) since it compares rates of phototransformation to experimental substrate uptakes (Figure 6c). We observe three distinct regions for the measured library: (1) low q_{24} low k_0 (MIL-125), (2) low q_{24} moderate k_0 (UCFMOF-2 and UCFMTV-3- $x\%$), and (3) moderate q_{24} high k_0 (UCFMTV-4- $x\%$). UCFMOF-2 shows the slowest turnover rate, both perhaps related to small pore windows that restrict transport. The UCFMTV-3- $x\%$ system shows slightly higher substrate loading and a faster turnover rate, related to better transport and access to the active sites given by the pore shape. The UCFMTV-4- $x\%$ system displays the largest uptake (about twice that of MIL-125) as well as much faster turnover rates. In particular, UCFMTV-4-30% has the highest turnover rate of the library, $k_0 = 1270 \text{ mmol}_{\text{BzOH}} \text{mol}_{\text{MOF}}^{-1} \text{h}^{-1}$ compared to MIL-125 $k_0 = 69.5 \text{ mmol}_{\text{BzOH}} \text{mol}_{\text{MOF}}^{-1} \text{h}^{-1}$ (Table S10). As we increase pore

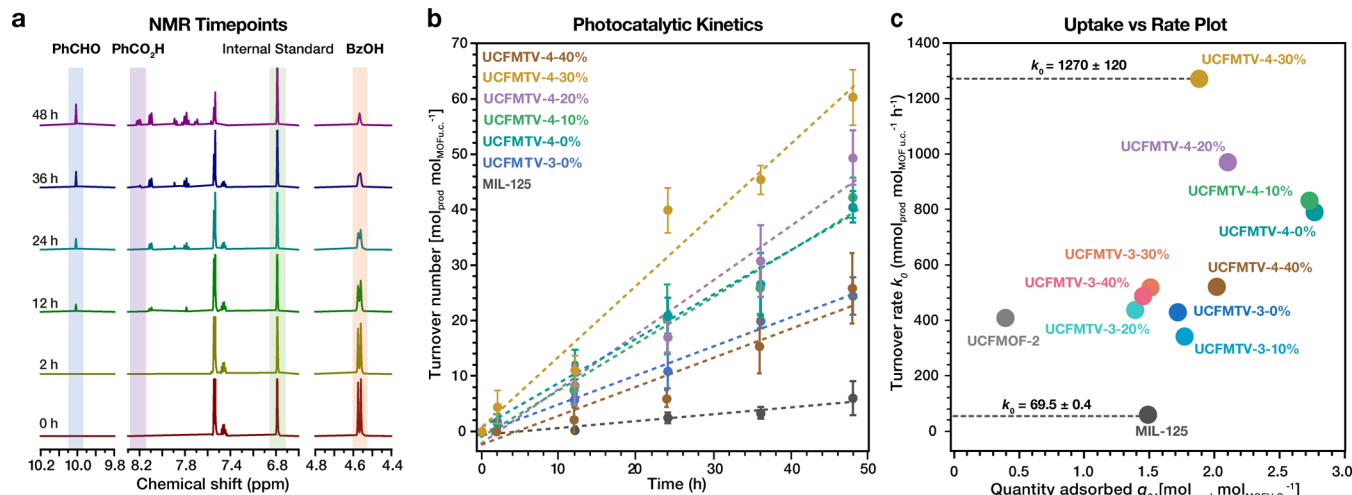


Figure 6. (a) Solution NMR spectra for each timepoint of photoredox catalysis from UCFMOF-4 with colored regions that indicate signals used for quantification. (b) Photocatalytic kinetic plots for MIL-125 (gray), UCFMTV-3-0% (blue), UCFMTV-4-0% (turquoise), -10% (green), -20% (purple), -30% (gold), and 40% (brown) broken line indicates pseudo-zero order linear fitting. (c) Structure–property relationship between MIL-125 and UCFMTVs with respect to uptake at 24 h (q_{24}) and photocatalytic turnover frequency k_0 . k_0 values of MIL-125 and UCFMTV-4-30% are shown.

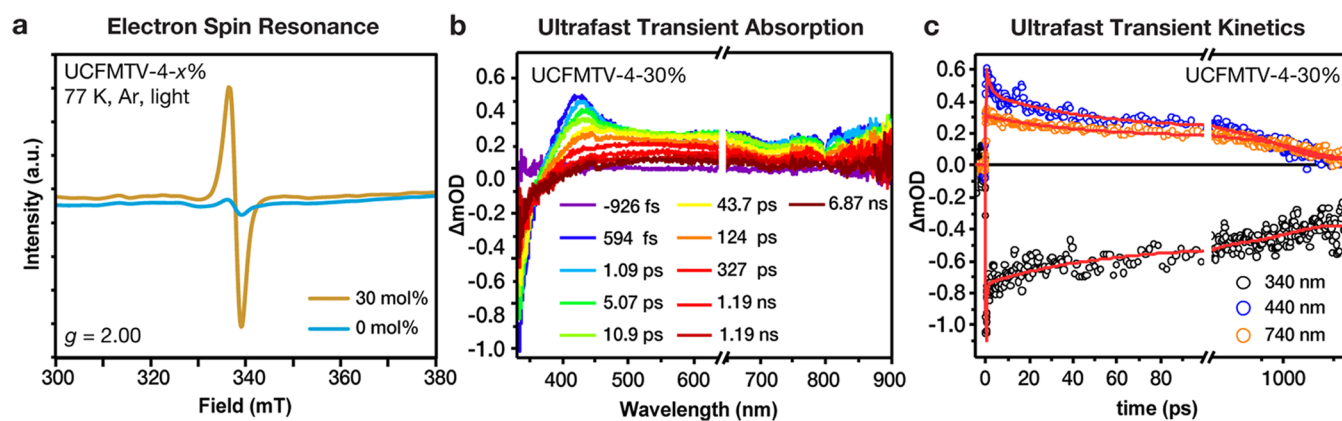


Figure 7. (a) Electron spin resonance (ESR) spectrum of UCFMTV-4-0% (blue) and UCFMTV-4-30% (gold) under an Ar atmosphere, at 77 K, after 30 min of irradiation with $\lambda > 385$ nm. (b) Ultrafast transient absorption spectrum of UCFMTV-4-30% in a solution of bis-amino-terminated poly(ethylene glycol) (PNH₂)/MeCN (see the SI) at increasing time delays (purple to red traces). (c) Kinetic traces of UCFMTV-4-30% at 340 nm (black symbols), 440 nm (blue symbols), and 740 nm (orange symbols). $\lambda_{\text{ex}} = 320$ nm, 120 $\mu\text{J cm}^{-2}$. The power used to excite the MOF sample was checked to ensure a linear response (Figure S72).

size and functionalization, the effects of loading and photo-transformation become more synergistic: Increasing amino content up to 30% decreases the substrate loading yet significantly increases the turnover rate (nearly double). Higher EDG content in UCFMTV-4-40% exhibited lower substrate capacity and lower turnover rate, perhaps related to increased defect sites, as we noted from optical spectroscopy (see above). Overall, UCFMTV-4-30% exhibits the fastest turnover rates in the library, 18 \times faster than MIL-125, demonstrating how steric and electronic effects can be tuned in a photocatalyst to optimize photocatalytic performance.

The thermal and structural stabilities of UCFMOFs were assessed by thermogravimetric and PXRD studies. All MOFs in the library are thermally stable up to 450 $^{\circ}\text{C}$ under N₂ flow and retain their bulk crystallinity after 48 h under photocatalytic conditions (Figures S83–S88), which are performed in open air under normal laboratory temperature and humidity. UCFMOFs and UCFMTVs also display remarkable shelf-life and postcatalytic stability, as shown by retention of bulk crystallinity beyond eight months of benchtop storage with no extra precautions taken to remove ambient air, moisture, or light (Figures S89–S91).

The generation of separated charge carriers (electrons and holes) is crucial to the development of photoredox catalysts. In titania MOFs, charge separation manifests itself as reduced Ti³⁺ sites and radical holes, the latter of which can be present on the carboxylate oxygens, a formally oxidized linker (radical cation) or on bridging oxygens within the SBU. This charge-separated state can be observed in two ways, i.e., via electron spin resonance (ESR) spectroscopy under steady state light irradiation and using ultrafast transient absorption UV–vis spectroscopy. ESR spectra of UCFMTV-4-0% and UCFMTV-4-30% (under an Ar atmosphere) are shown in Figure 7a after 30 min of Xe light irradiation. We observe the presence of paramagnetic signals consistent with spin 1/2 at 338 mT ($g = 2.00$) in both MOFs, with a significantly larger intensity in UCFMTV-4-30%. This indicates that 30% functionalization with amino groups produces a larger population of observable charge-separated states.

To further probe the charge-separated states relevant to photocatalysis, transient absorption spectroscopy (TAS) was employed. UCFMTV-4-30% was chosen as a model MOF for

study as exhibited the highest amount of oxidation products over time (Figure 6). Based on the electronic absorption spectra of H₂QPDC, DAQP (in ester form, compound S6), and UCFMTV-4-30% (Figure S68), we chose to excite the MOF with 320 nm as S6 absorbs at this wavelength, giving rise to the possibility of charge transfer occurring from the bound DAQP link to the [Ti₆O₉(CO₂)₆] $_{\infty}$ nanowire. It is important to note that the titania nanowire also absorbs at this wavelength, making selective excitation of the linker infeasible as spectral responses will include contributions from directly accessed [Ti₆O₉(CO₂)₆] $_{\infty}$ excited state(s). Conversely, H₂QPDC exhibits little to no absorption at 320 nm, so the resulting photophysics in UCFMTV-4-30% is expected to exclusively come from the [Ti₆O₉(CO₂)₆] $_{\infty}$ chain and DAQP. A more in-depth photophysical analysis of the MOF series will be presented in subsequent work.

Figure 7b,c shows the ultrafast transient absorption (TA) spectra and selected kinetics of UCFMTV-4-30% suspended in MeCN. Upon 320 nm excitation, the TA spectrum in Figure 7b exhibits a clear ground-state bleach of ~ 330 nm, a prominent excited-state absorption (ESA) feature with a λ_{max} of ~ 420 nm present at early times, and a broad absorption extending from 450 to 900 nm that hypsochromically shifts to higher energies over time and persists at the end of the instrumental time window. The bleach is consistent with the loss of ground-state carriers upon excitation. The relatively narrow ESA centered at 420 nm is consistent with the localized nature of vibrationally hot trapped holes on [Ti₆O₉(CO₂)₆] $_{\infty}$.^{45–47} The broad positive absorptions at 400–550 and 550–900 nm are primarily attributed to vibrationally relaxed or stabilized trapped holes (O^{•+} species) and electrons (Ti³⁺ species) along the chain, respectively.^{46–52} A typical indicator of an LMCT transition in MOFs is the presence of a linker radical cation in the TA spectra.^{14,24,53,54} The radical cation spectrum of S6 (DAQP diethyl ester) has absorptions at ~ 360 and 540 nm (Figure S69). Conversely, the spectral features for UCFMTV-4-30% are more so congruent with prior studies of photocatalytic TiO₂ systems,^{45,50,52,55–58} with little evidence for the presence of a DAQP^{•+} radical cation at $\lambda > 320$ nm excitation.

Representative kinetic traces are shown in Figure 7c and Table S10. The decays of the ground-state bleach at 340 nm

and holes at 440 nm have average lifetimes of 2 ± 1 , 60 ± 20 , and 1300 ± 500 ps, while the decay at 740 nm only exhibits the latter two lifetimes. The short-lifetime component observed at 340 and 440 nm is consistent with the decay of the vibrationally excited trapped holes (ESA at 420 nm) to a vibrationally relaxed state (broad absorption features). We expect such behavior, given that super-band gap excitation is known to result in vibrationally hot excited states that rapidly relax.⁵² The second component, with an average lifetime of 60 ± 20 ps, is likely associated with further vibrational relaxation to deeper trap sites along the $[\text{Ti}_6\text{O}_9(\text{CO}_2)_6]_\infty$ chain for both electrons and holes, consistent with the shifts in the spectral features.^{52,55,59} The third lifetime is attributed to the recombination of longer-lived trapped carriers.⁴⁵ Compared to UCFMOF-4 (Figures S69–S71, Table S9), the excited-state carrier lifetimes in UCFMTV-4-30% show an overall increase. The lifetime enhancement observed in UCFMTV-4-30% is attributed to the electron density that the amine groups provide to the carboxylate oxygen via induction. The added electron density is thought to stabilize the electron–hole pairs on the $\text{RCOO}^+ - \text{Ti}^{3+}$ bond and prolong recombination, similar to work by Kamat et al., on Li-intercalated TiO_2 .⁶⁰ The remainder of the signal after 7 ns (instrument time window) is composed of deeply trapped carriers on the $[\text{Ti}_6\text{O}_9(\text{CO}_2)_6]_\infty$ chain that decay on the nanosecond timescale and, therefore, are hypothesized to be responsible for photocatalysis when irradiated with >320 nm light. A simple reaction mechanism that is consistent with DFT calculations and spectroscopic and kinetic observations can be formulated, as described by the formation of a highly redox active charge-separated state from light excitation $[\text{TiO}_{1.5}(\text{O}_2\text{C}-\text{Ar})] + h\nu \rightarrow [(\text{Ti}^{\text{III}}\text{O}_{1.5})^+ - (\text{O}_2\text{C}-\text{Ar})^*]$, followed by redox quenching. More detailed studies on this mechanism with respect to excited-state lifetime electron transfer and MOF composition are underway.

CONCLUSIONS

In this study, we designed, synthesized, and characterized a library of photocatalytic MTV MOFs based on titania oxocarboxylate nanowire SBUs and linear oligo-*p*-phenylene dicarboxylate building blocks with the topology of rod-packed hex nets. Their isoreticular expansion as well as multivariate functionalization enabled the preparation of a library that probes the steric (pore sizes) and electronic (HOMO–LUMO gaps) traits toward uptake and photo-oxidation of benzyl alcohol. We observe that while the link expansion in UCFMOF-4 results in nearly doubling uptake compared to MIL-125, moderate amine functionalization results in an 18× increase in turnover rate in UCFMTV-4-30%. Our study found that when designing MOF photocatalysts, it is important to not only include light harvesting groups but also consider the uptake of substrates and the space available in the pores. Our current efforts focus toward studying the solvent and mass transport effects, other photoredox transformations of high synthetic value, and an in-depth mechanistic understanding of photocatalysis through the combination of time-resolved spectroscopy, electrochemical, and theoretical tools.

ASSOCIATED CONTENT

Supporting Information

The Supporting Information is available free of charge at <https://pubs.acs.org/doi/10.1021/jacs.2c12147>.

Experimental procedures for MOF synthesis; spectroscopic characterization; powder diffraction crystallography; pair distribution function analysis; scanning electron microscopy; thermal gravimetry; photocatalytic measurements, and theoretical calculations (PDF)

Accession Codes

CCDC 2072293–2072294 contain the supplementary crystallographic data for this paper. These data can be obtained free of charge via www.ccdc.cam.ac.uk/data_request/cif, or by emailing data_request@ccdc.cam.ac.uk, or by contacting The Cambridge Crystallographic Data Centre, 12 Union Road, Cambridge CB2 1EZ, UK; fax: +44 1223 336033.

AUTHOR INFORMATION

Corresponding Authors

Amanda J. Morris – Department of Chemistry, Virginia Tech, Blacksburg, Virginia 24061, United States; orcid.org/0000-0002-3512-0366; Email: ajmorris@vt.edu

Jose L. Mendoza-Cortes – Department of Chemical Engineering & Materials Science, Michigan State University, East Lansing, Michigan 48824, United States; Department of Chemical & Biomedical Engineering, Florida A&M—Florida State University, Department of Physics, Scientific Computing, Materials Science and Engineering, High Performance Materials Institute, Condensed Matter Theory, National High Magnetic Field Laboratory (NHMFL), Florida State University, Tallahassee, Florida 32310, United States; Present Address: J.L.M.-C. Department of Chemical Engineering & Materials Science, Michigan State University, East Lansing, Michigan 48824, United States.; orcid.org/0000-0001-5184-1406; Email: jmendoza@msu.edu

Titel Jurca – Department of Chemistry and Renewable Energy and Chemical Transformations Cluster, University of Central Florida, Orlando, Florida 32816, United States; orcid.org/0000-0003-3656-912X; Email: Titel.Jurca@ucf.edu

Karena W. Chapman – Department of Chemistry, Stony Brook University, Stony Brook, New York 11790, United States; orcid.org/0000-0002-8725-5633; Email: karena.chapman@stonybrook.edu

Fernando J. Uribe-Romo – Department of Chemistry and Renewable Energy and Chemical Transformations Cluster, University of Central Florida, Orlando, Florida 32816, United States; orcid.org/0000-0003-0212-0295; Email: fernando@ucf.edu

Authors

Jacob T. Bryant – Department of Chemistry and Renewable Energy and Chemical Transformations Cluster, University of Central Florida, Orlando, Florida 32816, United States; orcid.org/0000-0002-7737-4604

Matthew W. Logan – Department of Chemistry and Renewable Energy and Chemical Transformations Cluster, University of Central Florida, Orlando, Florida 32816, United States; orcid.org/0000-0002-8641-2043

Zhihengyu Chen – Department of Chemistry, Stony Brook University, Stony Brook, New York 11790, United States; orcid.org/0000-0001-5882-7076

Marcus Djokic – Department of Chemical Engineering & Materials Science, Michigan State University, East Lansing, Michigan 48824, United States; orcid.org/0000-0001-6504-9903

Daniel R. Cairnie – Department of Chemistry, Virginia Tech, Blacksburg, Virginia 24061, United States

Demetrius A. Vazquez-Molina – Department of Chemistry and Renewable Energy and Chemical Transformations Cluster, University of Central Florida, Orlando, Florida 32816, United States

A. Nijamudheen – Department of Chemical & Biomedical Engineering, Florida A&M—Florida State University, Department of Physics, Scientific Computing, Materials Science and Engineering, High Performance Materials Institute, Condensed Matter Theory, National High Magnetic Field Laboratory (NHMFL), Florida State University, Tallahassee, Florida 32310, United States; Present Address: A.N.: Chemistry Division, Brookhaven National Laboratory, Upton, New York 11973-5000, United States; orcid.org/0000-0001-9191-1851

Kyle R. Langlois – Department of Chemistry and Renewable Energy and Chemical Transformations Cluster, University of Central Florida, Orlando, Florida 32816, United States

Michael J. Markley – Department of Chemistry and Renewable Energy and Chemical Transformations Cluster, University of Central Florida, Orlando, Florida 32816, United States

Gisselle Pombar – Department of Chemistry and Renewable Energy and Chemical Transformations Cluster, University of Central Florida, Orlando, Florida 32816, United States

Ashley A. Holland – Department of Chemistry, University of Central Florida, Orlando, Florida 32816, United States

Jonathan D. Caranto – Department of Chemistry, University of Central Florida, Orlando, Florida 32816, United States; orcid.org/0000-0002-9196-5275

James K. Harper – Department of Chemistry and Biochemistry, Brigham Young University, Provo, Utah 84602, United States; orcid.org/0000-0001-8363-2019

Complete contact information is available at:
<https://pubs.acs.org/10.1021/jacs.2c12147>

Author Contributions

[†]J.T.B and M.W.L. contributed equally to this work.

Funding

Synthesis of materials and photocatalytic studies (CHE-1665277, FJU-R), solid-state NMR spectra acquisition (CHE-2016185, JKH) were supported by the National Science Foundation. Photophysical measurements were supported by the Department of Energy under Grant DE-SC0012446 (AJM). ESR measurements were supported by the U.S. Army (W911NF2010286, JDC and AAH).

Notes

The authors declare no competing financial interest.

ACKNOWLEDGMENTS

We acknowledge the UCF Advanced Research Computing Center and the High-Performance Computer cluster provided by ICER at MSU. This research used resources of the Advanced Photon Source; a U.S. Department of Energy (DOE) Office of Science User Facility operated for the DOE Office of Science by Argonne National Laboratory under contract no. DE-AC02-06CH11357. We also thank Prof. Michael O’Keeffe for helpful discussions.

ABBREVIATIONS

MOF metal–organic framework

1D	one-dimensional
3D	three-dimensional
DFT	density functional theory
SBU	secondary building unit
PDF	pair distribution function
DEF	<i>N,N</i> -diethylformamide
DMF	<i>N,N</i> -dimethylformamide
SEM	scanning electron microscopy
PXRD	powder X-ray diffraction
NMR	nuclear magnetic resonance
CP-MAS	cross-polarization magic angle spinning
BET	Brunauer–Emmett–Teller
NLDFT	nonlocal density functional theory
BzOH	benzyl alcohol
PhCHO	benzaldehyde
PhCO ₂ H	benzoic acid
LMCT	ligand-to-metal charge transfer
DR-UV–vis	diffuse reflectance ultraviolet–visible spectroscopy
MTV	multivariate
MeCN	acetonitrile
DATP	diamino terphenyl
DAQP	diamino quarterphenyl
GCMC	grand canonical Monte Carlo
ESR	electron spin resonance
TAS	transient absorption spectroscopy
BPDC	biphenyl dicarboxylate
TPDC	terphenyl dicarboxylate
QPDC	quarterphenyl dicarboxylate
EDG	electron-donating group

REFERENCES

- (1) Lang, X.; Zhao, J.; Chen, X. Cooperative photoredox catalysis. *Chem. Soc. Rev.* **2016**, *45*, 3026–3038.
- (2) Romero, N. A.; Nicewicz, D. A. Organic Photoredox Catalysis. *Chem. Rev.* **2016**, *116*, 10075–10166.
- (3) Prier, C. K.; Rankic, D. A.; MacMillan, D. W. C. Visible Light Photoredox Catalysis with Transition Metal Complexes: Applications in Organic Synthesis. *Chem. Rev.* **2013**, *113*, 5322–5363.
- (4) Schneider, J.; Matsuoka, M.; Takeuchi, M.; Zhang, J.; Horiuchi, Y.; Anpo, M.; Bahnemann, D. W. Understanding TiO₂ Photocatalysis: Mechanisms and Materials. *Chem. Rev.* **2014**, *114*, 9919–9986.
- (5) Li, Y.; Xu, H.; Ouyang, S.; Ye, J. Metal–organic frameworks for photocatalysis. *Phys. Chem. Chem. Phys.* **2016**, *18*, 7563–7572.
- (6) Assi, H.; Mouchaham, G.; Steunou, N.; Devic, T.; Serre, C. Titanium coordination compounds: from discrete metal complexes to metal–organic frameworks. *Chem. Soc. Rev.* **2017**, *46*, 3431–3452.
- (7) Keum, Y.; Park, S.; Chen, Y.-P.; Park, J. Titanium–Carboxylate Metal–Organic Framework Based on an Unprecedented Ti–Oxo Chain Cluster. *Angew. Chem., Int. Ed.* **2018**, *57*, 14852–14856.
- (8) Zhu, Y.-Y.; Lan, G.; Fan, Y.; Veroneau, S. S.; Song, Y.; Micheroni, D.; Lin, W. Merging Photoredox and Organometallic Catalysts in a Metal–Organic Framework Significantly Boosts Photocatalytic Activities. *Angew. Chem., Int. Ed.* **2018**, *57*, 14090–14094.
- (9) Yuan, S.; Liu, T.-F.; Feng, D.; Tian, J.; Wang, K.; Qin, J.; Zhang, Q.; Chen, Y.-P.; Bosch, M.; Zou, L.; Teat, S. J.; Dalgarno, S. J.; Zhou, H.-C. A single crystalline porphyrinic titanium metal–organic framework. *Chem. Sci.* **2015**, *6*, 3926–3930.
- (10) Nguyen, H. L.; Vu, T. T.; Le, D.; Doan, T. L. H.; Nguyen, V. Q.; Phan, N. T. S. A Titanium–Organic Framework: Engineering of the Band-Gap Energy for Photocatalytic Property Enhancement. *ACS Catal.* **2017**, *7*, 338–342.
- (11) Dan-Hardi, M.; Serre, C.; Frot, T.; Rozes, L.; Maurin, G.; Sanchez, C.; Férey, G. A New Photoactive Crystalline Highly Porous

Titanium(IV) Dicarboxylate. *J. Am. Chem. Soc.* **2009**, *131*, 10857–10859.

(12) Fu, Y.; Sun, D.; Chen, Y.; Huang, R.; Ding, Z.; Fu, X.; Li, Z. An Amine-Functionalized Titanium Metal–Organic Framework Photocatalyst with Visible-Light-Induced Activity for CO₂ Reduction. *Angew. Chem., Int. Ed.* **2012**, *51*, 3364–3367.

(13) Logan, M. W.; Lau, Y. A.; Zheng, Y.; Hall, E. A.; Hettinger, M. A.; Marks, R. P.; Hosler, M. L.; Rossi, F. M.; Yuan, Y.; Uribe-Romo, F. J. Heterogeneous photoredox synthesis of *N*-hydroxy-oxazolidinones catalyzed by metal–organic frameworks. *Catal. Sci. Technol.* **2016**, *6*, 5647–5655.

(14) Logan, M. W.; Ayad, S.; Adamson, J. D.; Dilbeck, T.; Hanson, K.; Uribe-Romo, F. J. Systematic variation of the optical bandgap in titanium based isoreticular metal–organic frameworks for photocatalytic reduction of CO₂ under blue light. *J. Mater. Chem. A* **2017**, *5*, 11854–11863.

(15) Hendon, C. H.; Tiana, D.; Fontecave, M.; Sanchez, C.; D'arras, L.; Sassoye, C.; Rozes, L.; Mellot-Draznieks, C.; Walsh, A. Engineering the Optical Response of the Titanium-MIL-125 Metal–Organic Framework through Ligand Functionalization. *J. Am. Chem. Soc.* **2013**, *135*, 10942–10945.

(16) Nasalevich, M. A.; Goesten, M. G.; Savenije, T. J.; Kapteijn, F.; Gascon, J. Enhancing optical absorption of metal–organic frameworks for improved visible light photocatalysis. *Chem. Commun.* **2013**, *49*, 10575–10577.

(17) Chambers, M. B.; Wang, X.; Ellezam, L.; Ersen, O.; Fontecave, M.; Sanchez, C.; Rozes, L.; Mellot-Draznieks, C. Maximizing the Photocatalytic Activity of Metal–Organic Frameworks with Aminated-Functionalized Linkers: Substoichiometric Effects in MIL-125-NH₂. *J. Am. Chem. Soc.* **2017**, *139*, 8222–8228.

(18) Deng, H.; Grunder, S.; Cordova, K. E.; Valente, C.; Furukawa, H.; Hmadeh, M.; Gandara, F.; Whalley, A. C.; Liu, Z.; Asahina, S.; Kazumori, H.; O'Keeffe, M.; Terasaki, O.; Stoddart, J. F.; Yaghi, O. M. Large-Pore Apertures in a Series of Metal–Organic Frameworks. *Science* **2012**, *336*, 1018–1023.

(19) Ockwig, N. W.; Delgado-Friedrichs, O.; O'Keeffe, M.; Yaghi, O. M. Reticular Chemistry: Occurrence and Taxonomy of Nets and Grammar for the Design of Frameworks. *Acc. Chem. Res.* **2005**, *38*, 176–182.

(20) Delgado-Friedrichs, O.; O'Keeffe, M.; Yaghi, O. M. Taxonomy of Periodic Nets and the Design of Materials. *Phys. Chem. Chem. Phys.* **2007**, *9*, 1035–1043.

(21) Eddaoudi, M.; Kim, J.; Rosi, N.; Vodak, D.; Wachter, J.; O'Keeffe, M.; Yaghi, O. M. Systematic Design of Pore Size and Functionality in Isoreticular MOFs and Their Application in Methane Storage. *Science* **2002**, *295*, 469–472.

(22) West, A. R. Solid Solutions. In *Solid State Chemistry and Its Applications*; Wiley and Sons, 1984.

(23) Wang, S.; Kitao, T.; Guillou, N.; Wahiduzzaman, M.; Martineau-Corcoss, C.; Nouar, F.; Tissot, A.; Binet, L.; Ramsahye, N.; Devautour-Vinot, S.; Kitagawa, S.; Seki, S.; Tsutsui, Y.; Briois, V.; Steunou, N.; Maurin, G.; Uemura, T.; Serre, C. A phase transformable ultrastable titanium-carboxylate framework for photoconduction. *Nat. Commun.* **2018**, *9*, No. 1660.

(24) Li, C.; Xu, H.; Gao, J.; Du, W.; Shangguan, L.; Zhang, X.; Lin, R.-B.; Wu, H.; Zhou, W.; Liu, X.; Yao, J.; Chen, B. Tunable titanium metal–organic frameworks with infinite 1D Ti–O rods for efficient visible-light-driven photocatalytic H₂ evolution. *J. Mater. Chem. A* **2019**, *7*, 11928–11933.

(25) Rosi, N. L.; Kim, J.; Eddaoudi, M.; Chen, B.; O'Keeffe, M.; Yaghi, O. M. Rod Packings and Metal–Organic Frameworks Constructed from Rod-Shaped Secondary Building Units. *J. Am. Chem. Soc.* **2005**, *127*, 1504–1518.

(26) Frot, T.; Cochet, S.; Laurent, G.; Sassoye, C.; Popall, M.; Sanchez, C.; Rozes, L. Ti₈O₈(OOCR)₁₆, a New Family of Titanium-Oxo Clusters: Potential NBUs for Reticular Chemistry. *Eur. J. Inorg. Chem.* **2010**, *2010*, 5650–5659.

(27) Nguyen, H. L.; Gándara, F.; Furukawa, H.; Doan, T. L. H.; Cordova, K. E.; Yaghi, O. M. A Titanium–Organic Framework as an

Exemplar of Combining the Chemistry of Metal– and Covalent–Organic Frameworks. *J. Am. Chem. Soc.* **2016**, *138*, 4330–4333.

(28) Toby, B. H.; Von Dreele, R. B. GSAS-II: the genesis of a modern open-source all purpose crystallography software package. *J. Appl. Crystallogr.* **2013**, *46*, 544–549.

(29) Palatinus, L.; Chapuis, G. SUPERFLIP - a computer program for the solution of crystal structures by charge flipping in arbitrary dimensions. *J. Appl. Crystallogr.* **2007**, *40*, 786–790.

(30) Pettersen, E. F.; Goddard, T. D.; Huang, C. C.; Couch, G. S.; Greenblatt, D. M.; Meng, E. C.; Ferrin, T. E. UCSF Chimera—a visualization system for exploratory research and analysis. *J. Comput. Chem.* **2004**, *25*, 1605–1612.

(31) Wang, C.; Liu, C.; He, X.; Sun, Z.-M. A cluster-based mesoporous Ti-MOF with sodalite supercages. *Chem. Commun.* **2017**, *53*, 11670–11673.

(32) Platero-Prats, A. E.; League, A. B.; Bernales, V.; Ye, J.; Gallington, L. C.; Vjunov, A.; Schweitzer, N. M.; Li, Z.; Zheng, J.; Mehdi, B. L.; Stevens, A. J.; Dohnalkova, A.; Balasubramanian, M.; Farha, O. K.; Hupp, J. T.; Browning, N. D.; Fulton, J. L.; Camaioni, D. M.; Lercher, J. A.; Truhlar, D. G.; Gagliardi, L.; Cramer, C. J.; Chapman, K. W. Bridging Zirconia Nodes within a Metal–Organic Framework via Catalytic Ni-Hydroxo Clusters to Form Heterobimetallic Nanowires. *J. Am. Chem. Soc.* **2017**, *139*, 10410–10418.

(33) BIOVIA. *Materials Studio Forcite*, v8.0.0.843; Dassault Systèmes: San Diego, 2014.

(34) Newsome, W. J.; Ayad, S.; Cordova, J.; Reinheimer, E. W.; Campiglia, A. D.; Harper, J. K.; Hanson, K.; Uribe-Romo, F. J. Solid State Multicolor Emission in Substitutional Solid Solutions of Metal Organic Frameworks. *J. Am. Chem. Soc.* **2019**, *141*, 786–790.

(35) Becke, A. D. Density-functional thermochemistry. III. The role of exact exchange. *J. Chem. Phys.* **1993**, *98*, 5648–5652.

(36) Lee, C.; Yang, W.; Parr, R. G. Development of the Colle-Salvetti correlation-energy formula into a functional of the electron density. *Phys. Rev. B* **1988**, *37*, 785–789.

(37) Janesko, B. G.; Henderson, T. M.; Scuseria, G. E. Screened hybrid density functionals for solid-state chemistry and physics. *Phys. Chem. Chem. Phys.* **2009**, *11*, 443–454.

(38) Grimme, S.; Antony, J.; Ehrlich, S.; Krieg, H. A consistent and Accurate *ab initio* Parametrization of Density Functional Dispersion Correction (DFT-D) for the 94 Elements H–Pu. *J. Chem. Phys.* **2010**, *132*, No. 154104.

(39) Garza, A. J.; Scuseria, G. E. Predicting Band Gaps with Hybrid Density Functionals. *J. Phys. Chem. Lett.* **2016**, *7*, 4165–4170.

(40) Walton, K. S.; Snurr, R. Q. Applicability of the BET Method for Determining Surface Areas of Microporous Metal–Organic Frameworks. *J. Am. Chem. Soc.* **2007**, *129*, 8552–8556.

(41) Sudik, A. C.; Côté, A. P.; Wong-Foy, A. G.; O'Keeffe, M.; Yaghi, O. M. A Metal–Organic Framework with a Hierarchical System of Pores and Tetrahedral Building Blocks. *Angew. Chem., Int. Ed.* **2006**, *45*, 2528–2533.

(42) Haerifar, M.; Azizian, S. Fractal-like Kinetics of Adsorption on Heterogeneous Solid Surfaces. *J. Phys. Chem. C* **2013**, *118*, 1129–1134.

(43) El Bardiji, N.; Ziat, K.; Naji, A.; Saidi, M. Fractal-like Kinetics of Adsorption Applied to the Solid/Solution Interface. *ACS Omega* **2020**, *5*, 5105–5115.

(44) BIOVIA. *Materials Studio Sorption*, v8.0.0.843; Dassault Systèmes: San Diego, 2014.

(45) Rossi, G.; Pasquini, L.; Catone, D.; Piccioni, A.; Patelli, N.; Paladini, A.; Molinari, A.; Caramori, S.; O'Keeffe, P.; Boscherini, F. Charge carrier dynamics and visible light photocatalysis in vanadium-doped TiO₂ nanoparticles. *Appl. Catal. B* **2018**, *237*, 603–612.

(46) Tamaki, Y.; Hara, K.; Katoh, R.; Tachiya, M.; Furube, A. Femtosecond Visible-to-IR Spectroscopy of TiO₂ Nanocrystalline Films: Elucidation of the Electron Mobility before Deep Trapping. *J. Phys. Chem. C* **2009**, *113*, 11741–11746.

(47) Zawadzki, P. Absorption Spectra of Trapped Holes in Anatase TiO₂. *J. Phys. Chem. C* **2013**, *117*, 8647–8651.

(48) Yoshihara, T.; Katoh, R.; Furube, A.; Tamaki, Y.; Murai, M.; Hara, K.; Arakawa, H.; Tachiya, M. Identification of Reactive Species in Photoexcited Nanocrystalline TiO₂ Films by Wide-Wavelength-Range (400–2500 nm) Transient Absorption Spectroscopy. *J. Phys. Chem. B* **2004**, *108*, 3817–3823.

(49) Sachs, M.; Pastor, E.; Kafizas, A.; Durrant, J. R. Evaluation of Surface State Mediated Charge Recombination in Anatase and Rutile TiO₂. *J. Phys. Chem. Lett.* **2016**, *7*, 3742–3746.

(50) Tamaki, Y.; Furube, A.; Murai, M.; Hara, K.; Katoh, R.; Tachiya, M. Dynamics of efficient electron-hole separation in TiO₂ nanoparticles revealed by femtosecond transient absorption spectroscopy under the weak-excitation condition. *Phys. Chem. Chem. Phys.* **2007**, *9*, 1453–1460.

(51) Tamaki, Y.; Furube, A.; Katoh, R.; Murai, M.; Hara, K.; Arakawa, H.; Tachiya, M. Trapping dynamics of electrons and holes in a nanocrystalline TiO₂ film revealed by femtosecond visible/near-infrared transient absorption spectroscopy. *C. R. Chim.* **2006**, *9*, 268–274.

(52) Triggiani, L.; Brunetti, A.; Aloï, A.; Comparelli, R.; Curri, M. L.; Agostino, A.; Striccoli, M.; Tommasi, R. Excitation-Dependent Ultrafast Carrier Dynamics of Colloidal TiO₂ Nanorods in Organic Solvent. *J. Phys. Chem. C* **2014**, *118*, 25215–25222.

(53) Santaclara, J. G.; Nasalevich, M. A.; Castellanos, S.; Evers, W.; Spoor, F. C.; Rock, K.; Siebbeles, D. A.; Kapteijn, F.; Grozema, F.; Houtepen, A.; Gascon, J.; Hunger, J.; van der Veen, M. A. Organic Linker Defines the Excited-State Decay of Photocatalytic MIL-125(Ti)-Type Materials. *ChemSusChem* **2016**, *9*, 388–395.

(54) de Miguel, M.; Ragon, F.; Devic, T.; Serre, C.; Horcajada, P.; Garcia, H. Evidence of photoinduced charge separation in the metal-organic framework MIL-125(Ti)-NH₂. *ChemPhysChem* **2012**, *13*, 3651–3654.

(55) Piccioni, A.; Catone, D.; Paladini, A.; O’Keeffe, P.; Boschi, A.; Kovtun, A.; Katsikini, M.; Boscherini, F.; Pasquini, L. Ultrafast Charge Carrier Dynamics in Vanadium-Modified TiO₂ Thin Films and Its Relation to Their Photoelectrocatalytic Efficiency for Water Splitting. *J. Phys. Chem. C* **2020**, *124*, 26572–26582.

(56) Qian, R.; Zong, H.; Schneider, J.; Zhou, G.; Zhao, T.; Li, Y.; Yang, J.; Bahnmann, D.; Hong Pan, J. Charge carrier trapping, recombination and transfer during TiO₂ photocatalysis: An overview. *Catal. Today* **2019**, *335*, 78–90.

(57) Furube, A.; Asahi, T.; Masuhara, H.; Yamashita, H.; Anpo, M. Charge Carrier Dynamics of Standard TiO₂ Catalysts Revealed by Femtosecond Diffuse Reflectance Spectroscopy. *J. Phys. Chem. B* **1999**, *103*, 3120–3127.

(58) Cowan, A. J.; Tang, J.; Leng, W.; Durrant, J. R.; Klug, D. R. Water Splitting by Nanocrystalline TiO₂ in a Complete Photoelectrochemical Cell Exhibits Efficiencies Limited by Charge Recombination. *J. Phys. Chem. C* **2010**, *114*, 4208–4214.

(59) Sun, J.; Yang, Y.; Khan, J. I.; Alarousu, E.; Guo, Z.; Zhang, X.; Zhang, Q.; Mohammed, O. F. Ultrafast Carrier Trapping of a Metal-Doped Titanium Dioxide Semiconductor Revealed by Femtosecond Transient Absorption Spectroscopy. *ACS Appl. Mater. Interfaces* **2014**, *6*, 10022–10027.

(60) Meekins, B. H.; Kamat, P. V. Got TiO₂ nanotubes? Lithium ion intercalation can boost their photoelectrochemical performance. *ACS Nano* **2009**, *3*, 3437–3446.

Recommended by ACS

Understanding Photocatalytic Activity Dependence on Node Topology in Ti-Based Metal–Organic Frameworks

Nikita Kolobov, Jorge Gascon, *et al.*

APRIL 17, 2023
ACS MATERIALS LETTERS

READ 

Molecular Engineering of Metal–Organic Layers for Sustainable Tandem and Synergistic Photocatalysis

Yingjie Fan, Wenbin Lin, *et al.*

FEBRUARY 08, 2023
JOURNAL OF THE AMERICAN CHEMICAL SOCIETY

READ 

Dynamic Bond-Directed Synthesis of Stable Mesoporous Metal–Organic Frameworks under Room Temperature

Youcong Li, Jing-Lin Zuo, *et al.*

APRIL 19, 2023
JOURNAL OF THE AMERICAN CHEMICAL SOCIETY

READ 

Titanium Sulfonate-Based Metal–Organic Frameworks

Dong-Fei Lu, Jian Zhang, *et al.*

MARCH 23, 2023
CRYSTAL GROWTH & DESIGN

READ 

Get More Suggestions >